Numerical Simulation Studies for Oceanic Anomalies in the North Pacific Basin: II. Seasonally Varying Motions and Structures

JOSEPH C. K. HUANG

Great Lakes Environmental Research Laboratory, NOAA, Ann Arbor, MI 48104, and Department of Atmospheric and Oceanic Sciences, The University of Michigan, Ann Arbor, MI 48109

(Manuscript received 14 March 1978, in final form 7 June 1978)

ABSTRACT

Seasonally varying currents and structures in the North Pacific Ocean are simulated by a baroclinic ocean model. The model has satisfactorily reproduced the gross nature of current systems and density fields as well as their seasonal variations in the North Pacific Ocean. The simulated fluctuations of oceanic transport have been found to be closely related to the imposed meridional movement of the atmospheric system. The vertically integrated transport is strong in late winter and early spring, with a maximum in the Kuroshio region of 63×10^6 m^3 s^{-1}, and weak in summer, with a minimum of about 33×10^6 m^3 s^{-1}. All three major circulation gyres, namely, the subtropic anticyclonic gyre, the subarctic and the tropic cyclonic gyres are intense in winter and broad and weak in summer. The subarctic gyre almost disappears from the North Pacific basin in July. The simulated equatorial undercurrent and countercurrent demonstrate significant seasonal changes. Both currents are strong but shallow in fall and winter, and weak but deep in spring and summer. The simulated surface temperature agrees with observations in midlatitudes, especially in summer, but it is higher than that observed in high latitudes during winter. In the tropics, westward propagating baroclinic long waves having wavelengths of about 11 000 km are also shown in the simulation.

Most of the poleward flow of heat energy is transported in the upper layers, especially the surface layer. The maximum heat transport occurs near 17°N in winter and near 25°N in summer.

The seasonal cycle of energetics shows that variations of the total barotropic energy follow the variations of the imposed winds with a lag of about one month and that the maximum baroclinic energy follows closely the maximum of the overall horizontal thermal gradient in the cooling cycle. This also confirms that the large-scale baroclinic current is generally in geostrophic balance.

Simulated results are compared with observational data whenever appropriate. General agreement is satisfactory. Discrepancies in comparisons are pointed out and improvements needed for the model are discussed.

1. Introduction

This is the second part of numerical simulation studies for oceanic anomalies in the North Pacific Basin. In a previous paper (Huang, 1978; hereafter referred to as I), the major objective of the simulation studies, namely, to investigate large-scale low-frequency fluctuations in the North Pacific Ocean in response to normal and anomalous meteorological conditions, was stated and the physical model was briefly described. Also the long-term mean state of the North Pacific Ocean under the annual mean atmospheric forcing was described. Certain dynamic and thermodynamic analyses in the model were demonstrated and some comparisons of model results with observed data were presented.

The ocean and atmosphere are continually varying and all oceanographic and atmospheric observational studies reveal temporally and spatially varying fields. Among the spectrum of variations in the atmosphere and ocean, the most dominant, low-frequency one is the seasonal cycle. Observations have shown that magnitudes of seasonal variations in currents are comparable to, in some places even greater than, the mean values. Though numerous studies have been devoted to oceanic responses to unsteady atmospheric forcing (e.g., Veronis and Stommel, 1956; Pedlosky, 1967; Lighthill, 1969), the seasonal varying circulation and density in the ocean remains poorly understood today.

Numerical simulation studies for seasonally varying motions and structures in a baroclinic ocean are still relatively few (Cox, 1970; Friedrich, 1970; Takano *et al.*, 1974; Bryan *et al.*, 1975), although ocean simulations are numerous (e.g., Gormatyuk and Sarkisyan, 1965; Bryan, 1969; Takano, 1969; O'Brien, 1971; Bryan and Cox, 1972; Haney, 1974; Bryan *et al.*, 1975). Studies by Cox (1970) and Freidrich (1970) were for the Indian Ocean and for the North Atlantic Ocean, respectively. Takano *et al.* (1974) studied the world ocean using a linear, flat-bottom model. They pointed out that in spite of

differences in grid size and in the shape of the bottom, there was no significant difference between the Indian Ocean circulation as reported by Cox (1970) and their results. Both models produced about the same seasonally varying equatorial currents and Somali Current.

The present study concerns the large-scale, seasonal variations in the North Pacific, with emphasis on understanding of the heat and momentum fluxes across the air-sea interface as well as within the upper layers of the ocean. A nonlinear baroclinic model possessing the actual coastal configurations of the North Pacific Ocean, but having a flat bottom, is used to carry out the seasonal simulation. This paper is devoted to a description of the simulated seasonally varying motions and structures in the North Pacific Ocean. This seasonal state will be used as the model climatology to investigate the dynamics of large-scale thermal anomalies in the North Pacific Ocean for the subsequent study.

2. Description of the model

The North Pacific Ocean model and its annual mean climatology were described in I. The model is based on the primitive equations with essentially all major physical processes incorporated, including nonlinear advection terms. Temperature and salinity are predicted from the conservation equations. Since the model is designed for the study of large-scale low-frequency motions in the ocean, external gravity waves are filtered out by the rigid-lid approximation. Other simplifications of the model are the hydrostatic assumption, the Boussinesq approximation with respect to the density variations and a closure approximation of eddy viscosities for subgrid-scale motions. The horizontal grid separation for the whole North Pacific domain is 2.5° in both latitude and longitude. There are 10 variable-thickness layers in the vertical, seven layers of which are located above the main thermocline. The total depth is constant at 4 km. No-slip and insulation conditions are applied to all solid boundaries and a free-slip condition is applied at the equatorial boundary. The transport streamfunction is constant on all boundaries, including the equator. The velocity and density in the ocean are produced by the climatologically prescribed, seasonally varying surface wind and a set of atmospheric variables, such as insolation, air temperature, humidity, cloudiness, etc., which couple with the oceanic surface temperature to determine the surface heat flux. Though bottom topographic effects are neglected, there is still a small amount of energy exchange between the barotropic mode (the vertical mean velocity) and the baroclinic mode (the deviation of the horizontal velocity from its vertical mean) due to the nonlinear effects. Horizontal and vertical eddy viscosities are 2.5×10^8 and 1.5 $cm^2 s^{-1}$, respectively, while diffusivities are 10^7 and 1 $cm^2 s^{-1}$, respectively. A time step of 4.2 h is used throughout time integrations of this study. There are five prognostic variables in the model, namely, the horizontal components of the shear current u', v', the vertically integrated streamfunction ψ, temperature T and salinity S, and there are three diagnostic variables, viz., the vertical component of velocity w, the pressure field p and the density field ρ. For numerical schemes and detailed information about computations (see Huang, 1978).

Note that ignoring the bottom topography in the present study may involve errors in the transport functions (e.g., Holland, 1967). However, we are more interested in the large-scale, seasonal variations and, at a later stage, in the anomalous phenomena existing in the upper shallow layers of the ocean where the baroclinic velocity and seasonally varying heat contents are not markedly affected by topography (Gill and Niiler, 1973). More serious limitations of the model are that no wind-stirred mixed layer and no mesoscale eddy dynamics are included. Thus the results from the present model, with known weaknesses, are being compared with available observations in order to establish a level of simulation skill from which improved models with more realistic parameterizations can be developed.

3. Initial state, boundary conditions and time integrations

The initial state of the ocean model in this study is the quasi-equilibrium state obtained after 60 years of time integrations under the annual mean atmospheric forcing. As shown in I, the model has demonstrated its ability to portray the large-scale mean circulation patterns and mean density field in the North Pacific Ocean. Comparisons show favorable agreement between the simulated currents, temperature and salinity distributions and the available observational data.

In the present seasonal simulation, all prescribed seasonally varying atmospheric forcing parameters, as described in I, are fed into the model ocean at the time step of every model day. The seasonally varying climatological data were obtained as follows. Monthly values of the surface air temperature, vapor pressure and zonal and meridional geostrophic winds were obtained from a data tape for the Northern Hemisphere Climatological Atlases of Taljaard *et al.* (1974) and Jenne *et al.* (1974) from the National Center for Atmospheric Research. Monthly values of cloud cover were obtained from Miller and Feddes (1971) and the solar radiation from List (1963). These data were provided to us by Dr. R. L. Haney at the Naval Postgraduate School.

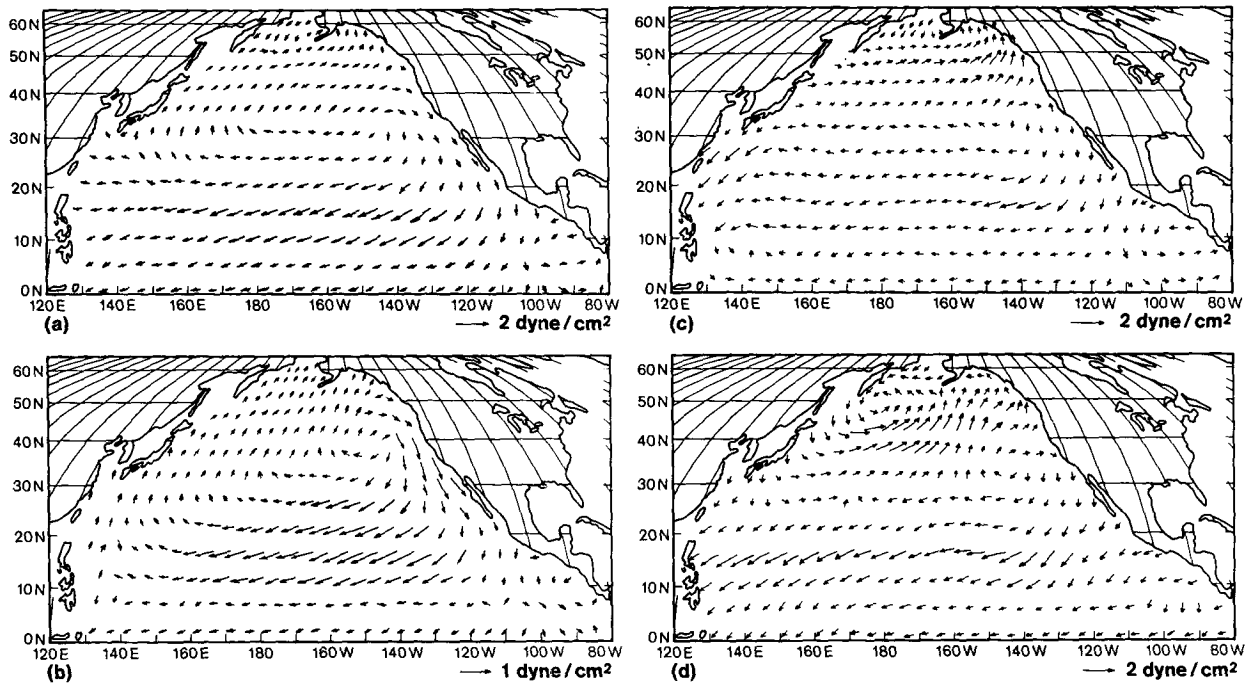

FIG. 1. Vector plots of surface wind stresses for four typical days to represent four seasons for (a) 15 April (spring), (b) 15 July (summer), (c) 15 October (fall), (d) 15 January (winter).

These seasonally varying atmospheric variables were Fourier analyzed and only the first three harmonics of the annual cycle were retained for forcing the ocean. Statistics show that more than 95% of variances are within the first three pairs of Fourier coefficients. The zeroth coefficients of the seasonal forcing functions were replaced by the annual mean part of the atmospheric forcing used in the mean state integrations to eliminate possible discrepancies between two atmospheric data sources. Note that there are no time-dependent evaporation and precipitation data available to be imposed as the seasonal upper boundary condition for the prediction of salinity. Therefore, the annual mean evaporation and precipitation data for integrations of the mean oceanic state are also used for the seasonal simulation.

Surface wind stresses and heat fluxes are computed using bulk aerodynamic formulas with the continuously varying climatological atmospheric parameters and the model-predicted sea surface temperature, as described in I. Fig. 1 consists of vector plots of surface wind stresses for four typical days at the middle of their respective seasons: 15 April (Fig. 1a) represents the spring season; 15 July (Fig. 1b), the summer; 15 October (Fig. 1c), the fall and 15 January (Fig. 1d), the winter. This representative presentation is used throughout this study. Notice that in Fig. 1 (as in some other figures) scales selected automatically by the plotting routine are different in Fig. 1b, where 1 dyn cm^{-2} is used, from the other three graphs, where 2 dyn cm^{-2} are used. Note also that half of the data points were filtered out in all vector plots due to the same reason. Fig. 1 shows that the winter wind stress (Fig. 1d) is much stronger than that of the summer (Fig. 1b), especially in the high-latitude region. The seasonal monsoon effect is clearly indicated in the wind distributions in summer and in winter along the continental coastal regions and in the subtropic western Pacific in particular. The northwest winds along the California coast are stronger in spring and summer than in winter.

Time integrations for the seasonal simulation of the North Pacific Ocean under the time-varying atmospheric forcing were carried out for about 15 years. Based on the most active mechanism in the density adjustment, namely, the vertical advection, the characteristic time scale for a layer depth scale of about 1000 m with a moderate vertical velocity of about 0.5 m day^{-1} is about 6 years. We realize that lower layers are *not* in quasi-equilibrium with the seasonally varying boundary conditions after 15 years of integration. However, since the mean basis of seasonally varying forcing functions was the long-term annual mean values with which the ocean spun up to a quasi-equilibrium state, the seasonal effect at deep layers should be small. Based on scale analysis as well as on observational data, seasonal variations are mostly confined to the upper several hundred meters from the surface. Numerical model studies also indicated that there are little or no

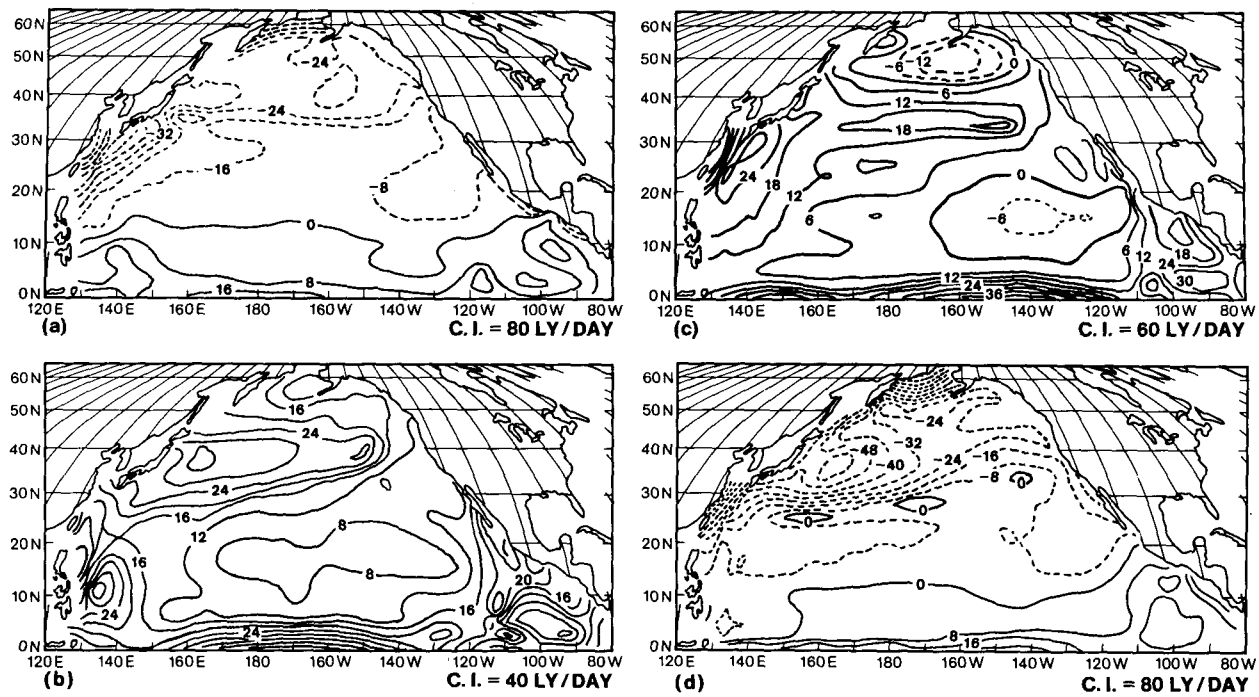

FIG. 2. Net downward heat flux at the surface during the 15th year of integration for (a) spring, contour interval in 80 ly day^{-1}; (b) summer, contour interval in 40 ly day^{-1}; (c) fall, contour interval in 80 ly day^{-1}; (d) winter, contour interval in 80 ly day^{-1}. (Note: 1 ly day^{-1} = 4.84433 × 10^{-5} W cm^{-2}).

temperature changes in response to the seasonal variations below 300 m depth in the ocean (Wetherald and Manabe, 1972). As will be shown later, the time-dependent varying motions and structures in the ocean have demonstrated a seasonal quasi-equilibrium state in the model for the last few years, with a secular change of less than 6% of the annual variation.

Net downward heat fluxes computed from the continuously varying climatological atmospheric data and the predicted sea surface temperatures for the 4 typical days are plotted in Fig. 2. Away from the equatorial region, where it is always being directly heated, the ocean generally receives heat energy from the atmosphere during summer and early fall, while it feeds energy back to the atmosphere in winter and early spring. As shown in Fig. 2, the most active heat exchange region in the North Pacific Ocean is in the midlatitudes northeast of Japan, where a maximum seasonal variation of 1200 ly day^{-1} (0.058 W cm^{-2}) is indicated. The magnitudes and distribution pattern of the computed heat fluxes generally agree well with observational seasonal variations of heat exchanges in the North Pacific Ocean (Wyrtki, 1973). A slight discrepancy in heat fluxes between the model computations and those of Wyrtki (1973) based on observed data may exist in the phase relation. The former heating or cooling occurs about 10–15 days earlier than the latter.

4. Discussion of results

In this section, the simulated seasonal variations from the North Pacific Ocean model are presented. The North Pacific Ocean is bounded by the huge Eurasian continent in the north and west, by the North American continent in the north and east and by the South Pacific Ocean in the south. The domain of interest to us is from the equator to 65°N in latitude and from 120°E to 80°W in longitude. Three prevailing wind zones, namely, the tropic trades, the subtropic westerlies and part of the Arctic easterlies, exist in the area. Monsoon effects are also strong in the coastal region, especially over the Southeast Asian water. In winter in the Northern Hemisphere, the Intertropical Convergence Zone (ITCZ) is at its southernmost position (around 2°N) and atmospheric highs form over the continents and lows over the oceans. Asiatic highs and Aleutian lows dominate the area. During summer in the Northern Hemisphere the ITCZ lies at its northernmost position (~15°N) and lows are formed over the continents. Pacific highs and Asiatic lows dominate the area. Ocean circulations in the upper layer of the North Pacific undergo considerable variations in response to the shifting of the major wind system. Wyrtki (1965) and Tsuchiya (1974) found a good correlation between the positions of the North Equatorial Countercurrent and the ITCZ. Meyers (1975) and White (1977) correlated the sea-

sonal variations in transport in the North Equatorial Current region and in the midlatitude Pacific to the wind field.

a. The vertically integrated transport

In a coarse grid ocean model such as the NORPAX model the nonlinear effects in the momentum equations are relatively small, except near the equator and at the western boundary. The vertically integrated streamfunction in the ocean approximately satisfies the Sverdrup relation for most of the area. Fig. 3 shows transport streamflows on the four representative days previously indicated. Since the seasonal migration amplitude of the equatorial trough is from 5°S to 12°N, centered in the Northern Hemisphere most of the year, it has just crossed the equator in early spring (15 April). The ITCZ lies about 2–4°N and the wind system in the North Pacific shifts from strong to moderate, moving northward. The trade wind region occupies the area from the Tropic of Cancer to the equator and a small portion of arctic easterly shows up in the northernmost latitudes in the North Pacific Ocean as shown in Fig. 1a. As shown in Fig. 3a, a typical three gyral circulation is simulated in the North Pacific Ocean in response to the spring wind shown in Fig. 1a. The middle one is a subtropic anticyclonic gyre with a maximum transport in the Kuroshio region of about 49 $\times$ 10^6 m^3 s^{-1} and two are cyclonic gyres in the tropic and subarctic region with transports of 38 $\times$ 10^6 m^3 s^{-1} and 15 $\times$ 10^6 m^3 s^{-1}, respectively. As the season progresses to summer, the wind over the North Pacific is weaker than at any other season (Fig. 1b). The oceanic circulation in summer (Fig. 3b) maintains a pattern similar to that in spring but all three gyres are relatively weaker. The subarctic gyre almost disappears. In fall the trades expand latitudinally to near 20°N in the western tropics due to the shift of the monsoon and the strength of the subarctic easterly also increases. As shown in Fig. 3c, the tropic gyre is the broadest of all seasons and the transport of the subarctic gyre increases to about 25 $\times$ 10^6 m^3 s^{-1}, while the subtropic anticyclonic gyre remains similar in strength to that in spring. Winds are much stronger in winter (Fig. 1d) and all gyral circulations are strengthened, as shown in Fig. 3d. The subtropic anticyclonic gyre has a maximum transport near the Kuroshio region of about 63 $\times$ 10^6 m^3 s^{-1}. The tropic gyre increases its maximum transport to about 46 $\times$ 10^6 m^3 s^{-1} and the subarctic gyre to about 33 $\times$ 10^6 m^3 s^{-1}. Note that the subarctic gyre extends farther southward to 36°N along the Asiatic coast in the winter and more subtropic warm water flows northeastward into the Gulf of Alaska. As predicted by linear theory, the transport function of the model follows the pattern of the vertical component of the curl of wind stress. The simulated Kuroshio transport agrees well with the world ocean simulation of Takano *et al.* (1974).

It is rather difficult to compare the simulated transport, such as the Kuroshio, the Oyashio and the North Equatorial Current, etc., with observa-

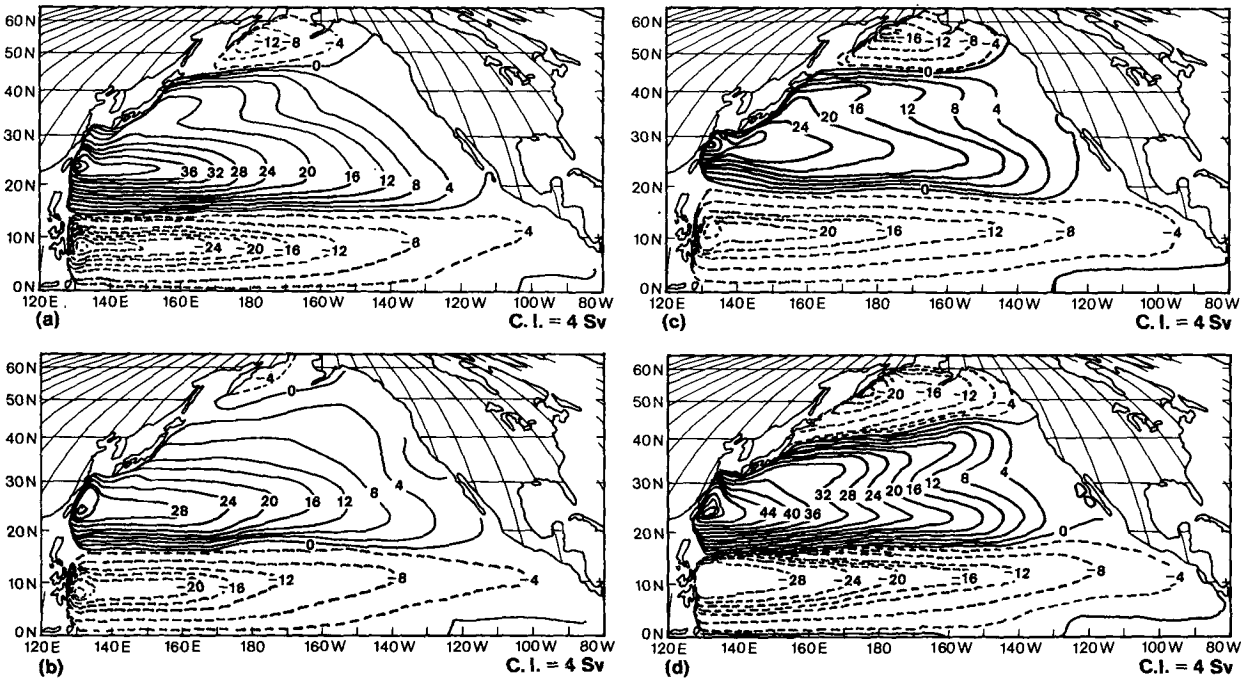

FIG. 3. Seasonal variation of the transport streamfunction for (a) spring, (b) summer, (c) fall, (d) winter.

tional data. There always exists the problem of the width scale used for estimating the transport from current measurements and the problem of selecting the reference levels of no motion for the relative transport calculations from the observational data. However, insights into model verification are gained through comparisons with observed data in spite of these difficulties.

The most prominent phenomenon in the North Pacific Ocean is the Kuroshio Current in the subtropic anticyclonic gyre. Taft (1972) calculated the transport in the region south of Japan (130–141°E) relative to 800 db and found a maximum in his third quarter (1 August–15 September) with no significant differences between the first, second and fourth quarters. Pavlova [1964 (from Taft, 1972)] computed the average transport around 135°E relative to 1500 db and found no obvious maximum in transport in either August or September. Based on volume transport calculations relative to 1000 db for 32 sections across the Kuroshio near 135°E, Masuzawa (1972) stated that there is marginal evidence that there are two maxima per year: one in spring and the other in fall. Wyrtki (1961) computed the geostrophic volume transport relative to 800 db in the southwest Pacific south of 25°N and indicated that the Kuroshio east of Taiwan shows the highest transport in April and the lowest in December. The simulated integrated streamfunction in the Kuroshio region shows a relatively high transport in April and the lowest in November and early December, which agrees with Wyrtki's (1961). However, the maximum simulated transport occurs in late winter, January-February. There is no available observational data showing such a maximum in winter. As to the magnitude of the Kuroshio, Taft (1972) showed the relative transport around 139°E to be about 42×10^6 m^3 s^{-1} all year round, except during August–September when it is about 25% higher. Nitani (1972) indicated that the transport of the Kuroshio east of Taiwan is about 40×10^6 m^3 s^{-1}, and that of the Kuroshio south of the Kii Peninsula is about 65×10^6 m^3 s^{-1} on the average. The simulated Kuroshio agrees quantitatively well with these observational values. Worthington and Kawai (1972), based on three deep sections across the Kuroshio in August and September of 1965, stated that volume transports of the Kuroshio in the Ryukyu, in the Shikoku and in the Inubozuki sections are 59, 84 and 88×10^6 m^3 s^{-1}, respectively, considerably larger than indicated by the model simulation. As Takano *et al.* (1974) pointed out, there is not enough reliable seasonal observational data to estimate the Kuroshio transport so that comparisons can be made comfortably with the simulated result.

In the tropic cyclonic gyre that composes all the equatorial currents, the simulated North Equatorial Current system across 130°E (estimated from 10 to 20°N) shows a maximum transport of about 72×10^6 m^3 s^{-1} in winter (January–February) and about 64, 46 and 44×10^6 m^3 s^{-1} in spring, summer and fall, respectively, with an annual average of about 56×10^6 m^3 s^{-1}. Sverdrup *et al.* (1942) estimated that the transport of the North Equatorial Current is about 45×10^6 m^3 s^{-1}. Wyrtki (1961) estimated it to be 38×10^6 m^3 s^{-1}; Masuzawa (1972), 48×10^6 m^3 s^{-1} and Nitani (1972), 70×10^6 m^3 s^{-1} near 130°E and 53×10^6 m^3 s^{-1} at 137°E. The simulated seasonal transports of the North Equatorial Current agree qualitatively with these observed values. Based on the trade wind zone oceanography study data, Meyers (1975) stated that the mean monthly values of westward volume transport near 150°W, from 11.5 to 20.5°N, have a maximum in fall ($\sim 24 \times 10^6$ m^3 s^{-1}) and a minimum in spring (about 12×10^6 m^3 s^{-1}). Simulated transports of the North Equatorial Current around 150°W do show a relative maximum in fall (40×10^6 m^3 s^{-1}) and a minimum in early summer (25×10^6 m^3 s^{-1}). However, simulated transports are about 50% higher than Meyers' values.

The simulated subarctic cyclonic gyre shows strong seasonal fluctuation, from about 30×10^6 m^3 s^{-1} in winter to about 4×10^6 m^3 s^{-1} in summer. Reid's (1973) analysis of the Boreas Exploration showed 23×10^6 m^3 s^{-1} in winter (relative to 1500 db) and Allen's (1964) estimation is about 8×10^6 m^3 s^{-1} for summer in the Kamchatka Current region. Further south in the Oyashio region, Hata's (1965) data show a southward transport across 43°N of about 3×10^6 m^3 s^{-1} in winter and about 2×10^6 m^3 s^{-1} in spring and summer. The simulated transport in the Kamchatka current region agrees satisfactorily with Reid (1973) and Allen (1964). The simulated transport in the Oyashio region also agrees qualitatively well with Hata's (1965), except for winter.

b. The velocity

The surface layer current (10 m) is shown in Fig. 4. It is mostly dominated by the Ekman drift, which quickly responds to the wind. Most of the major observed currents are portrayed in the model simulation. In the midlatitude region from subtropic to subarctic, the Kuroshio and the Oyashio, which merge north of 40°N, form the beginning of the west drift North Pacific Current. Near the North American coast, the North Pacific Current splits into the Alaska Current flowing northward and the California Current flowing southward. The Alaska Current connects to the Aleutian Current, which passes across the Aleutian Islands, instead of flowing along the Aleutian Chain, due to the simplification of the model geometry. The Aleutian Current flows

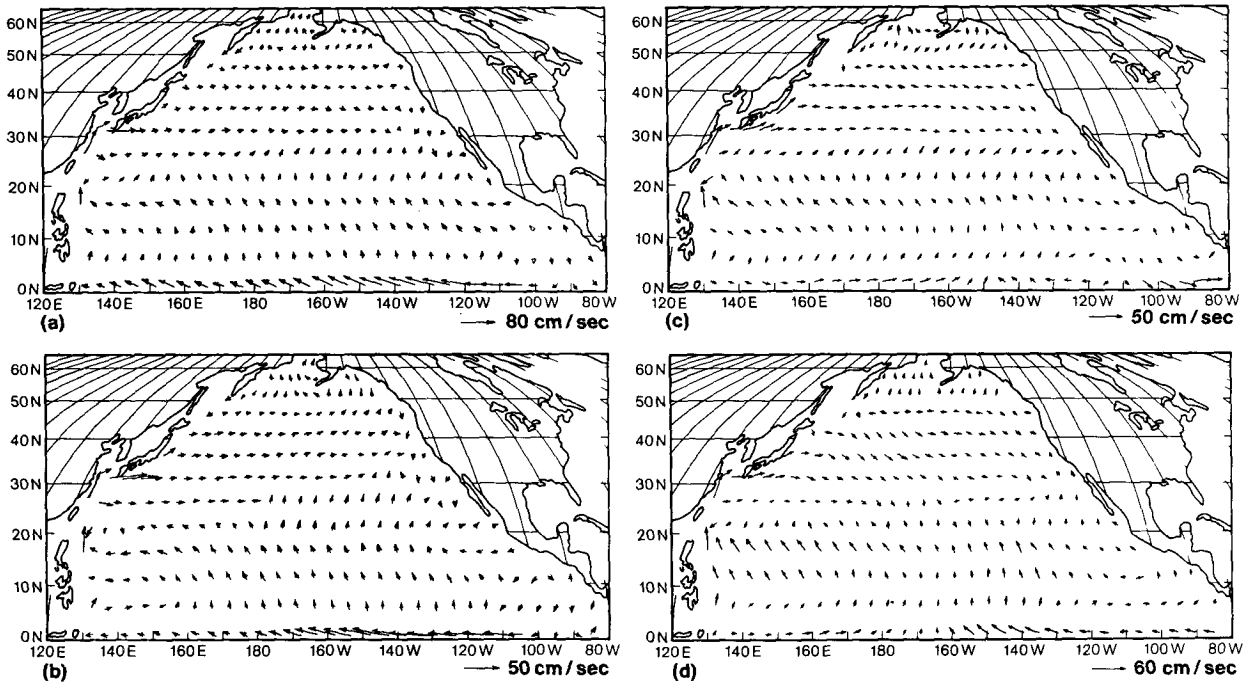

FIG. 4. Simulated current velocity at 10 m for (a) spring, vector scale in 80 cm s^{-1}; (b) summer, vector scale in 50 cm s^{-1}; (c) fall, vector scale in 50 cm s^{-1}; (d) winter, vector scale in 60 cm s^{-1}.

into the Bering Sea and connects to the Kamchatka Current and the Oyashio to complete the subarctic gyral circulation. The southward weak California Current joins the beginning of the North Equatorial Current flowing westward. The North Equatorial Current branches northward into the Kuroshio and southward to join the Equatorial Countercurrent, which is more clearly discerned in fall and winter, as shown in Figs. 4c and 4d. Note that the simulated equatorial countercurrent lies south of 2.5°N near the equator, instead of at 5–10°N latitudes where it is generally observed. The South Equatorial Current, which flows westward near the equator, exists in the North Pacific Ocean during spring and summer, but disappears from the Northern Hemisphere in the West Pacific during fall and winter, as indicated in Fig. 4.

Simulated currents in the open ocean are for the most part strong in the equatorial region and relatively weak in the mid-latitude region. In addition to the stronger wind stress in the tropics than that in the midlatitude, it is also expected from the overall dynamic balance in the ocean that, in the tropic zone, the Ekman current will generally enforce the geostrophic flow induced by the north-south density gradient, while it opposes the geostrophic flow in the mid-latitude. The surface current in the Kuroshio region is essentially quite steady all year round, with a relative maximum of 64 cm s^{-1} in fall and about 60 cm s^{-1} in other seasons. However, the simulated maximum current is located south of Japan instead of along the Japanese coast, probably due to the simplification in bottom topography. The simulated Kamchatka current and the Oyashio are much stronger during winter (6–10 cm s^{-1}) than in summer (1–2 cm s^{-1}).

Taft (1972) analyzed the seasonal variations of surface current speed in the Kuroshio south of Japan from 130° to 135°E and from 135° to 140°E, based on shiplog data. His curves are reproduced in Fig. 5, together with the simulated curves at two appropriately comparable points. All four curves are rather similar; even the slightly downstream phase difference (~1 month) between the curves at different locations is accurately simulated by the model. However, the simulated current speed is about 50% lower than the observed speed and it has no minimum in May.

The most noticeable seasonal variation simulated is in the equatorial region, where the surface current is mostly the South Equatorial Current under the influence of the southeast trade wind. The strongest westward surface current occurs in spring near 140°W, where the velocity reaches 75 cm s^{-1} (Fig. 4a). Intense upwelling, as will be shown later, is also present in this region due to the divergence of Ekman transport in the surface layer. The South Equatorial Current disappears to the west of 160°W in fall and winter when the Equatorial Countercurrent is clearly indicated.

Wyrtki (1965) and Tsuchiya (1974) indicated that the variation of the North Equatorial Countercur-

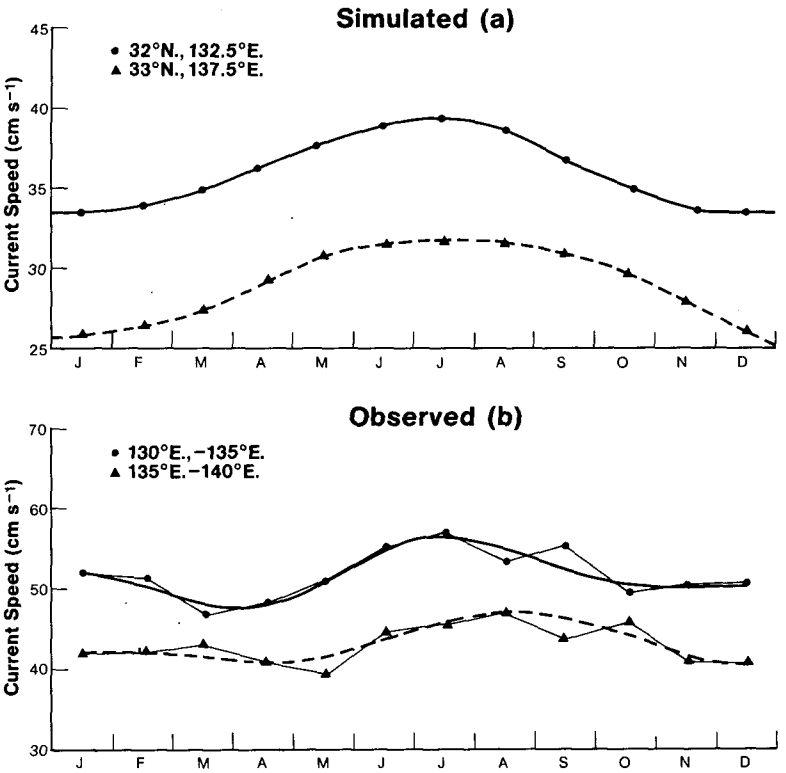

FIG. 5. Simulated (a) and observed (b) (Taft, 1972) seasonal variations of surface current speeds for two areas in the Kuroshio south of Japan

rent is closely related to the shift of the ITCZ in the major wind system. In the eastern tropic Pacific Ocean, the countercurrent is discontinuous or nonexistent in spring when the ITCZ lies near its southernmost position (at latitude 2–6°N) and it is strong, broad and extended east to the coast of Costa Rica in fall when the ITCZ lies near its northmost position (at latitude 11–15°N). The maximum surface speed of the Equatorial Countercurrent is generally observed in September (~40 cm s^{-1}). The simulated seasonal variation of the Equatorial Current agrees well with the observed seasonal phase relationship. However, the simulated current speed is generally about 50% lower than the observed current speed.

Along the west coast of the North American Continent, the California Current generally flows southeastward. However, when the southerly wind is dominating the west coast during fall and winter, the implications for the existence of the Davidson Countercurrent flowing northwestward near the coast are clearly indicated in the simulated current (Figs. 4c and 4d).

The simulated seasonal shift of the California Current and the appearance of the California Countercurrent in fall and winter support Wyrtki (1965) and Schwartzlose and Reid (1971) in their contention that the California Current flows strongly southeastward parallel to the coast in spring and summer and that the flow is mostly weak and offshore in fall and winter, while the northwestward Davidson Current appears south of 27°N when the wind is shifted primarily from the south in the coastal area.

Simulated seasonal current patterns of the third layer in the model at a depth of 60 m are shown in Fig. 6. Over most of the North Pacific Ocean, currents remain similar to these of the surface layer, except that the Ekman deflecting effect is greatly reduced and the geostrophic influence is correspondingly increased. The current flows mostly in the zonal direction. The strongest current of this layer is the simulated Kuroshio Current in spring, which has a value of 49 cm s^{-1}. The major difference between these currents and those at the surface is in the equatorial currents. During spring, some indications for the formation of an Equatorial Undercurrent are shown in the west tropic Pacific west of 170°E as the current starts to flow eastward south of the Phillippine Sea. As the season progresses, the eastward flow extends further eastward, reaching 160°W in summer, and nearly across the entire basin during fall and winter (reaching 100°W in fall and 130°W in winter). The eastward Undercurrent is clearly discerned for all four seasons in the deeper layers at 225 m depth as shown in Fig. 7. During

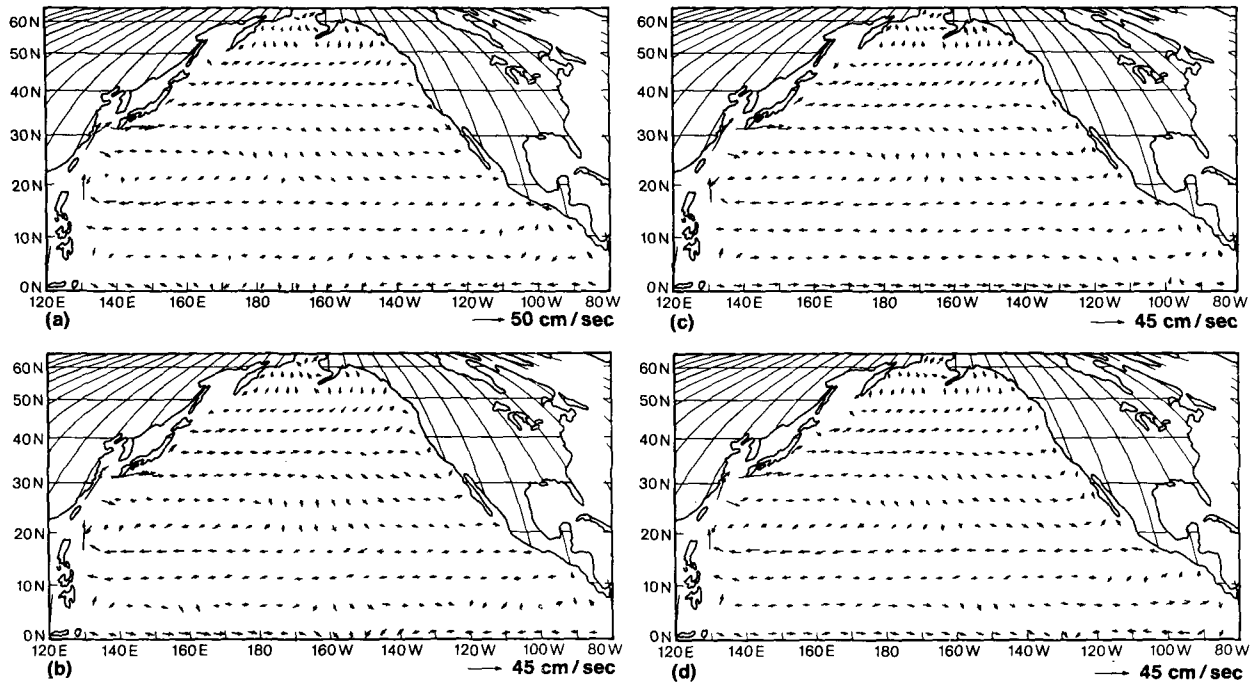

FIG. 6. As in Fig. 4 except for the third layer at 60 m.

spring and summer, there is eastward flow across the entire basin on the equator, while the eastward flow is weaker and broken in sections during fall and winter. This implies that the model Undercurrent is deep in the spring and summer (especially summer) and is shallow in the fall and winter. The same conclusion can be applied to the simulated Equatorial Countercurrent since it behaves rather similarly to the model Undercurrent (unfortunately it was filtered out in the vector plotting). Dynamic analyses support the conclusions of Meyers (1975) that, in the fall, in response to the Ekman pumping

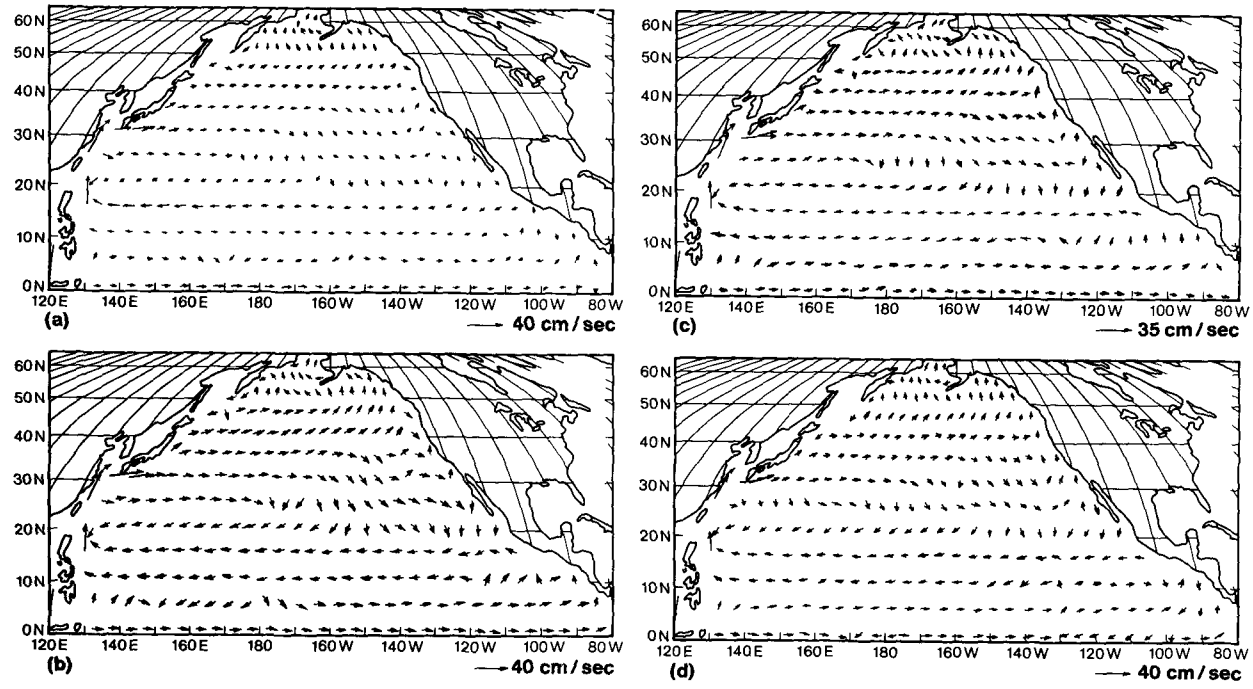

FIG. 7. As in Fig. 4 except for 225 m.

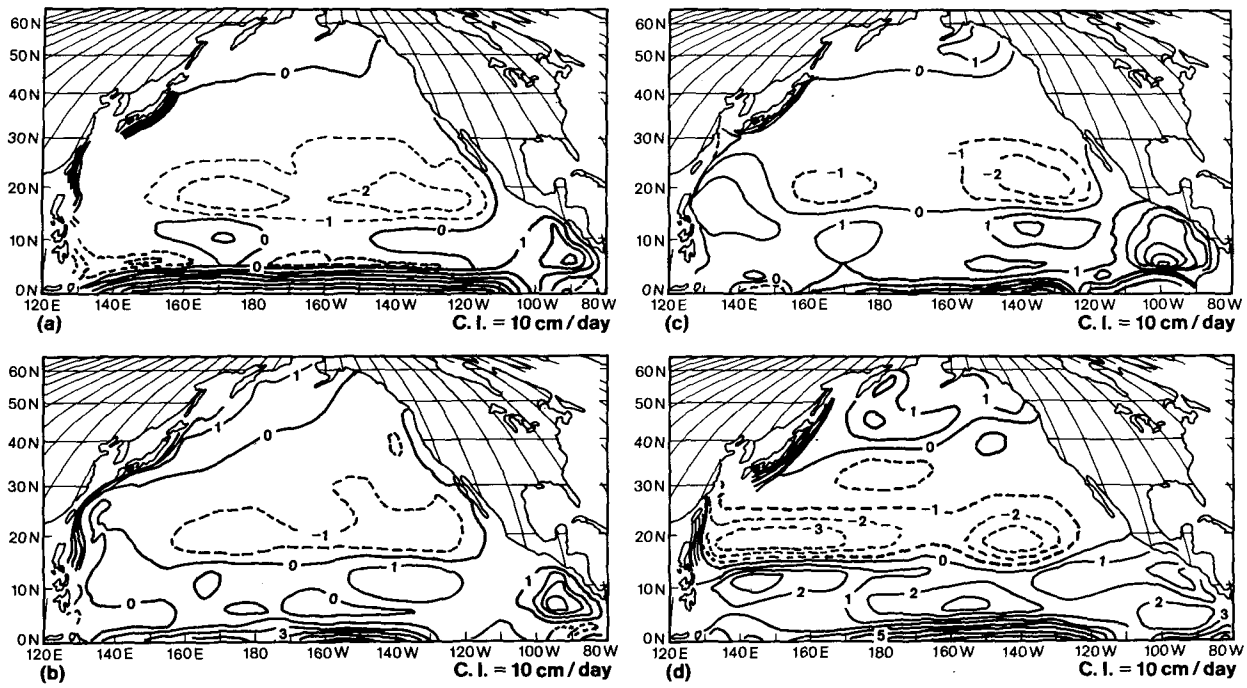

FIG. 8. Vertical velocity below the surface layer (at 20 m depth) for (a) spring, (b) summer, (c) fall, (d) winter. Solid contour line indicates upwelling; dotted line, downwelling. Contour interval in 10 cm day^{-1}.

around 10°N, the thermocline is shallow and the thermal gradient is sharp, resulting in a strong Countercurrent in the upper shallow layers. In the spring the thermocline is deep, resulting in a deeper Countercurrent.

Along the North American coast, the simulated California Current flows southward near the continent in spring and summer and shifts outward to the open ocean during fall and winter, while a northward, Davidson Countercurrent exists close to the coast at this depth north of Baja California (Figs. 7c and 7d).

There is very little seasonal variation shown below 700 m depth. The simulated Kuroshio is still strong (~15 cm s^{-1}) but the Equatorial Undercurrent is not detectable. At deep layers (below 1000 m depth) an abyssal creep flowing southward in the west Pacific is apparent and the southward current under the Kuroshio reaches 4 cm s^{-1}.

The model simulated vertical velocity at 20 m depth is shown in Fig. 8. In the open ocean, this is mostly due to Ekman pumping, which is related to the curl of wind stress. Intense upwellings occur in the equatorial region and along the western boundary in all seasons. The intense upwelling along the equator does not penetrate very deep, but that at the western boundary does. There are always downwellings in the eastern tropic region near the Costa Rica Dome, but upwellings at the coast. There are general broad weak downwellings in the subtropic region and upwellings in the subarctic region. The strongest upwelling occurs in spring (~2 × 10^{-3} cm s^{-1}) in the central equator. In spring the active upwelling zone extends to about 5°N in the tropic region and a broad, weak downwelling zone is found from subtropic to subarctic region. Upwellings and downwellings are generally weak in summer and become more intense in fall. Downwelling in the subtropic region and upwelling in the subarctic region are strong during the winter season. Note that there is a distinct seasonal oscillation in the upwelling along the west coast of North America with a maximum in summer.

There are three Ocean Weather Stations (OWS) in the North Pacific that have been monitored for long periods of time. Their long record of data, especially on temperature, is invaluable for deducing statistically meaningful seasonal variations for their representative areas. OWS *Victor* (34°N,164°E) is located in the western subtropic east of Kuroshio. OWS Papa (50°N,145°W) is in the eastern midlatitude and OWS *November* (30°N,140°W) is in the eastern subtropic in the North Pacific Ocean. The simulated seasonal variations of transport functions (Fig. 1a), velocities (Fig. 1b), surface current speeds (Fig. 1c), temperatures (Fig. 1d), the observed temperature (Fig. 1e) and the imposed climatology of the wind stress curls (Fig. 1f) at three locations are plotted as shown in Figs. 9, 10 and 11. The observational data are obtained from Ballis (1973).

At OWS *Victor*, the model currents, both at the surface layer and at the fifth layer about 150 m below

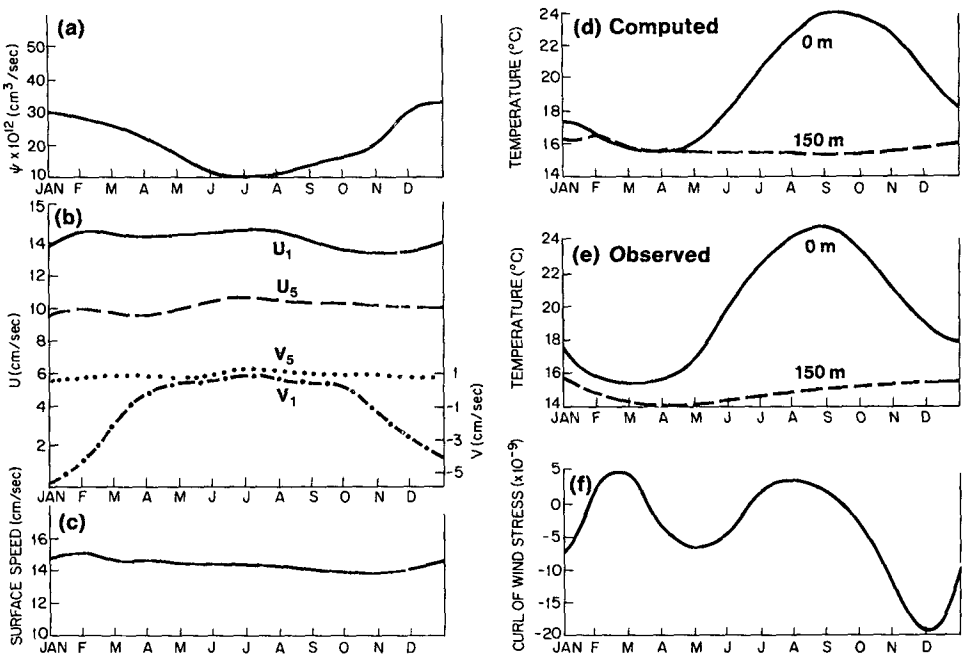

FIG. 9. Seasonal variations of (a) the simulated transport, (b) the simulated velocity at 10 m and at 150 m, (c) the simulated surface speed, (d) the simulated temperature, (e) the observed temperature (Ballis, 1973) and (f) the specified curl of wind stresses (in 10^{-9} dyn cm^{-3}) at OWS *Victor*.

the surface, are rather steadily eastward (Figs. 9b and 9c). The northward surface component varies slightly in response to the wind stress, which is strong during winter. Transport is strong during winter and weak during summer. The negative wind stress curl is intense in winter, correlating with the strong winter transport, and the wind stress curl is weak in summer, correlating generally with the weak summer flow. Nevertheless, the correlations are not equally obvious, being less apparent in summer. It is probable that the flow near the *Victor* station is still under the influence of the Kuroshio and its meandering because there the local wind stress curl bears no relation to the transport of the boundary current.

OWS *Papa* is located near the eastern end of the

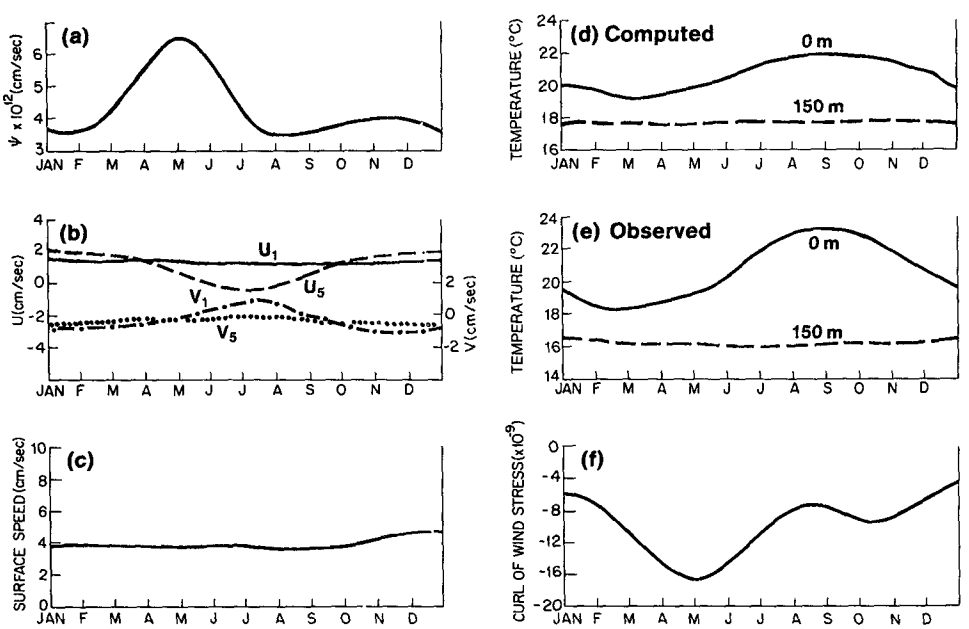

FIG. 10. As in Fig. 9 except at OWS *Papa*.

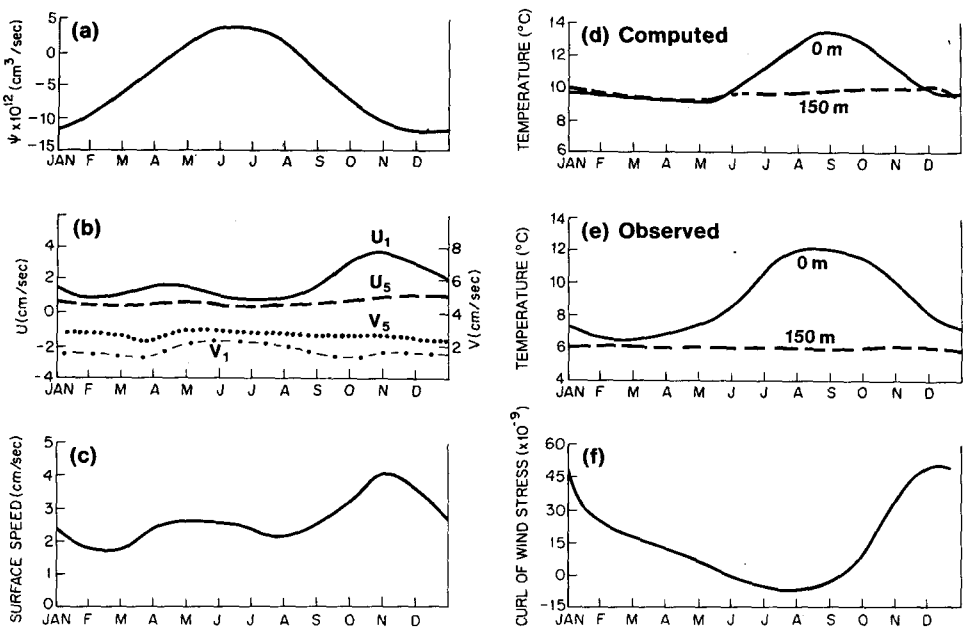

FIG. 11. As in Fig. 9 except at OWS *November*.

North Pacific Current, where it begins to split north and south. A close inverse correlation between the surface wind stress curl and the cyclonic transport is found at this location as indicated in Figs. 10a and 10f. The summer transport is very weak as the positive wind stress curl is almost null. Currents are generally weak throughout the year, with a weak maximum in late fall and early winter.

OWS *November* is south of the *Papa* station on the eastern side of the subtropic anticyclonic gyre. Here again a good correlation is found between the negative wind stress curl and the anticyclonic transport. Currents are weak but steady toward the southeast. There are not many current or transport measurements available at these stations for comparison with the simulated results. However, the long and continuous temperature records provide valuable verification of the model, discussed in the next paragraph.

c. *Temperature field*

The most important single parameter in the ocean to interact with the atmosphere is the sea surface temperature. The simulated surface layer temperatures for 15 February, representing the coldest month, and of 15 August, representing the warmest month, are shown in Figs. 12a and 12b. The general pattern of simulated temperatures and their variation from winter to summer closely resembles the observed pattern. In general, there are stronger temperature gradients in the midlatitudes, a broad warm band of water in the western tropic region, an isolated warm zone in the eastern tropic region near Costa Rica and an equatorial cool zone from the Central American coast to the central North Pacific Ocean. In winter the sharp horizontal temperature gradient zone exists from 25 to 45°N in the western North Pacific, while in summer it is pushed northward more than 10° latitude and the meridional gradient is further strengthened around 40°N. The broad warm water in the western North Pacific extends to 32°N in summer, but is limited to south of 20°N in winter. The mean observed surface temperatures for February and for August are also reproduced in Figs. 12c and 12d. While there is general agreement between the simulated and the observed surface temperature patterns, especially during summer, the simulated winter temperatures in the subarctic region and the summer temperatures in the tropic region are warmer than observed.

Below the surface layer, the seasonal fluctuations in temperature are similar to these of the surface but with decreased amplitude and some phase shift in time. Such seasonal fluctuations are more easily examined at the OWS locations where observations are available for comparisons.

Seasonal variations of the simulated and observed temperatures at the surface and at 150 m for the three ocean stations (*Victor, Papa, November*) are shown in Figs. 9, 10 and 11. In the western subtropics (*Victor*) the agreement between the simulated surface temperature and the mean observed surface temperature is very good both in magnitude and phase of the annual cycle. At 150 m depth, the agreement is satisfactory, except that the amplitude is smaller in the simulation. At OWS *Papa*, the

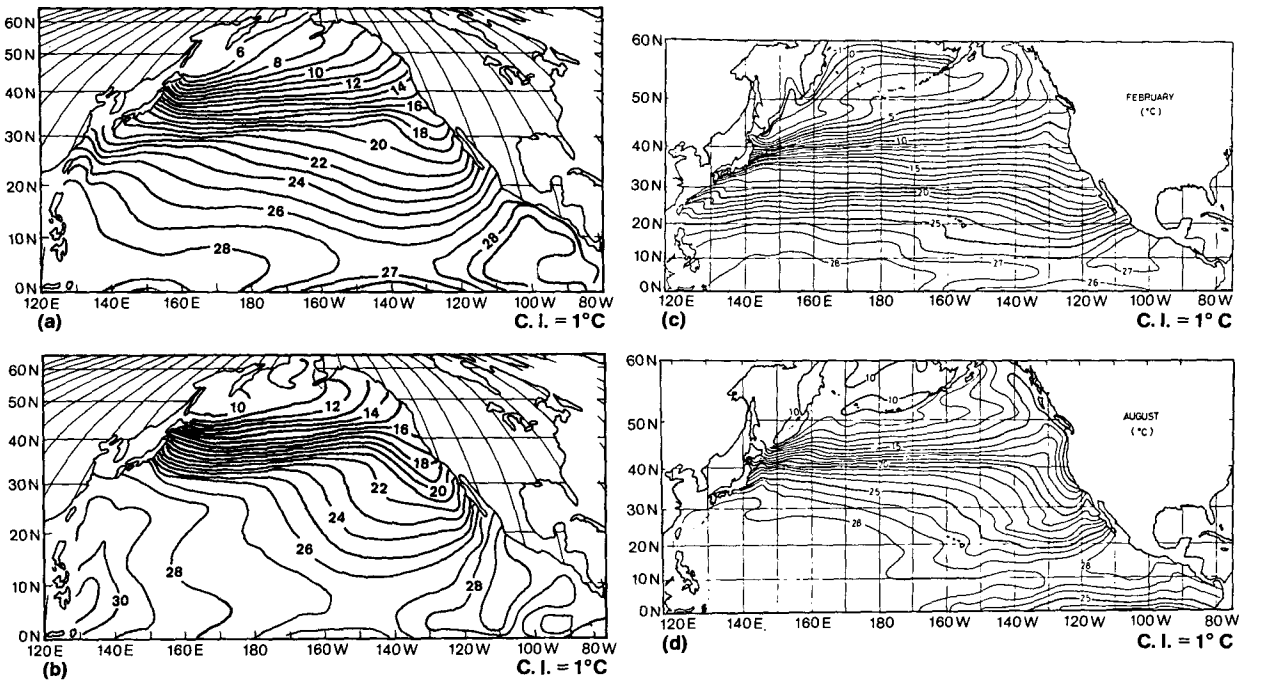

FIG. 12. Simulated and observed (Masuzawa, 1972) surface temperature in the North Pacific Ocean for (a) simulated February, (b) simulated August, (c) observed February, (d) observed August.

simulated annual cycle is also in good agreement with the observed except that the amplitude is smaller than the observation and the mean temperature is somewhat warmer. At OWS *November*, the agreement between the simulated and observed temperature at the surface and 150 m is fairly good, although, again, the amplitude in the seasonal cycle is slightly smaller and the 150 m temperature is slightly warmer in the simulation. Seasonal variations of sea surface temperature at two locations published by Wyrtki (1965), one in the mid-latitude eastern and the other in the tropic western North Pacific Ocean, were also compared with the corresponding points simulated in the model. In both cases, the phase and amplitude of the annual cycle compare satisfactorily with the observation.

The seasonal variation of the monthly mean temperature along the section from San Francisco to Honolulu is reproduced from the monthly report of the National Marine Fisheries Service (NMFS), as shown in Fig. 13. The observed temperature data are obtained from ships-of-opportunity. The corresponding simulated temperature for the representative days are shown in Fig. 14. As indicated in Figs. 13 and 14, the gross features show some resemblance. The thermocline is deep in winter and spring, shallow in summer and fall. The temperature is warm near Honolulu and cool near San Francisco. The isotherms are inclined up from the tropics to the midlatitudes. However, the major deficiencies are the lack of an explicit seasonal thermocline and the excessive thickness of the permanent thermocline simulated in the model. This produces a relatively constant vertical temperature gradient from the surface down to 500 m and results in a much higher temperature in the intermediate water level. The simulated temperature at 500 m is about 5°C higher than observed, while the simulated surface temperature is in good agreement with the observed. This deficiency is obviously due to the lack of effective thermocline dynamics in the model.

There are no meaningful observational data available in the subarctic region for comparison with the model. However, it appears that the simulated temperatures in the subarctic region are generally too high during winter and the amplitude of the seasonal temperature change is smaller than observed. A scrutiny of the initial condition and the seasonal variation of temperature leads us to believe that the discrepancies are probably attributable to two deficiencies in the simulation. The first is the summer (warm) bias of the atmospheric forcing data of the annual mean ocean model as noted in I. The second is the non-equilibrium state in the density field due to insufficient annual cycles in the seasonal integrations. The simulated annual mean surface temperature, reported in I, is very similar in both magnitude and pattern to the August surface temperature in the seasonal simulation. The simulated January surface temperature in high latitudes is much lower than the annual mean surface temper-

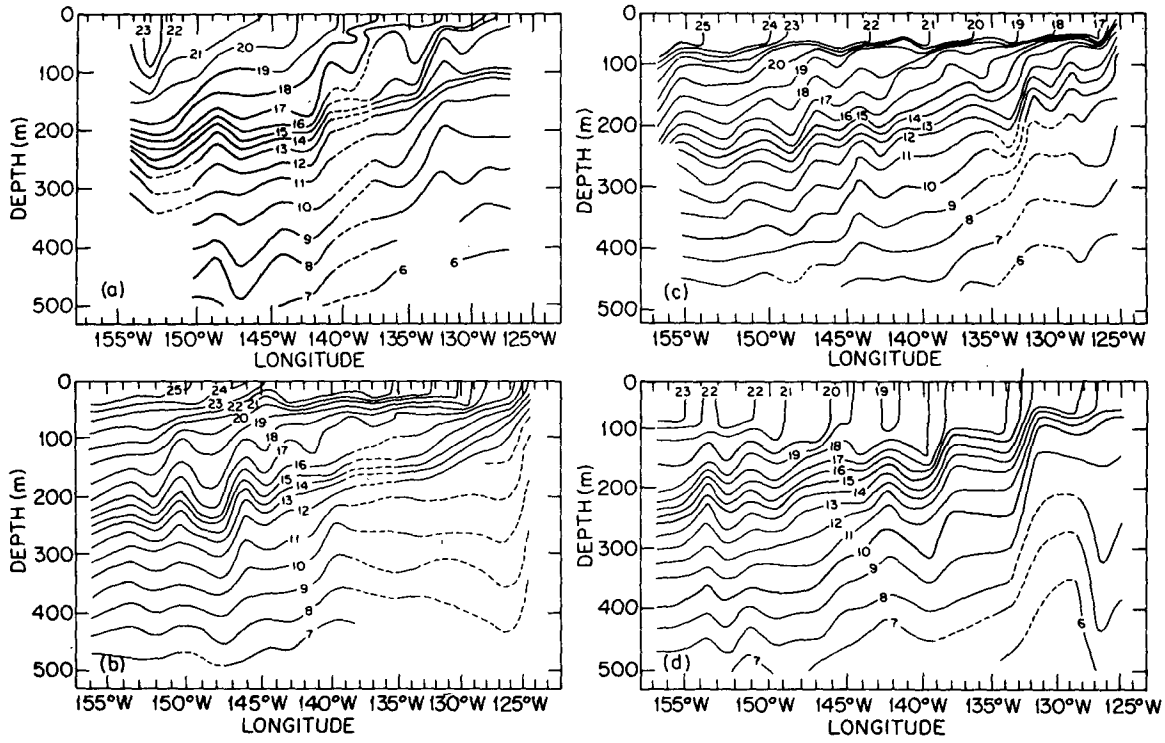

FIG. 13. Observed temperature (°C) along the section from San Francisco to Hawaii (from NOAA/NMFS report) for (a) spring, (b) summer, (c) fall, (d) winter.

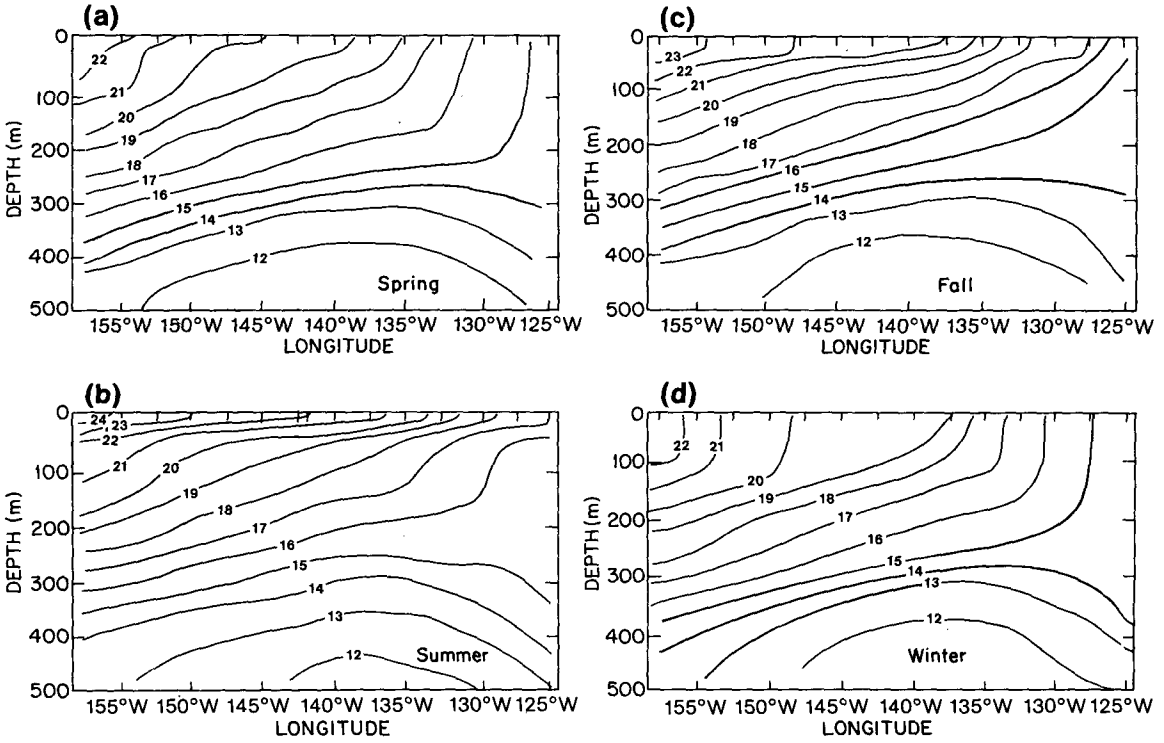

FIG. 14. Simulated temperature (°C) along the section from San Francisco to Hawaii for (a) spring, (b) summer, (c) fall, (d) winter.

ature. This indicates that the seasonal atmospheric forcing has gradually lowered the temperature at high latitudes. However, the seasonal ocean model has not reached an equilibrium state after 15 annual cycles of integrations. This is indicated by the excessive feedback of heat energy from the high latitude area in the North Pacific Ocean, as shown in Fig. 2d, and by the existence of a remaining moderately strong vertical temperature gradient in the high latitude water column. Though the convective adjustment mechanism in the model accelerates the internal cooling process (Wetherald and Manabe, 1972), which eventually cools the surface temperature in high latitudes to approximately the temperature of the bottom water, it decelerates the external cooling in high latitudes by reducing the heat loss from the ocean to the atmosphere, which depends mostly on air-sea temperature differences.

d. Heat transport

The poleward transport of heat from the tropics to high latitudes and its seasonal fluctuations in the ocean are important questions connected with global energy balance in the climate study. Heat is transported from low latitudes to high latitudes by the meridional component of velocity, which is partitioned into a barotropic mode and a baroclinic mode, and by horizontal diffusion due to the existence of the meridional temperature gradients. As pointed out in I, contributions from the barotropic current to the total heat energy transport are relatively small. Seasonal heat energy transports in the model are shown in Fig. 15. As the meridional current is strongest in winter, the heat transport by advection then is the highest of all seasons, at a maximum about 6×10^{14} cal s^{-1} (2.51×10^{15} W) centered around 15°N. In spring the

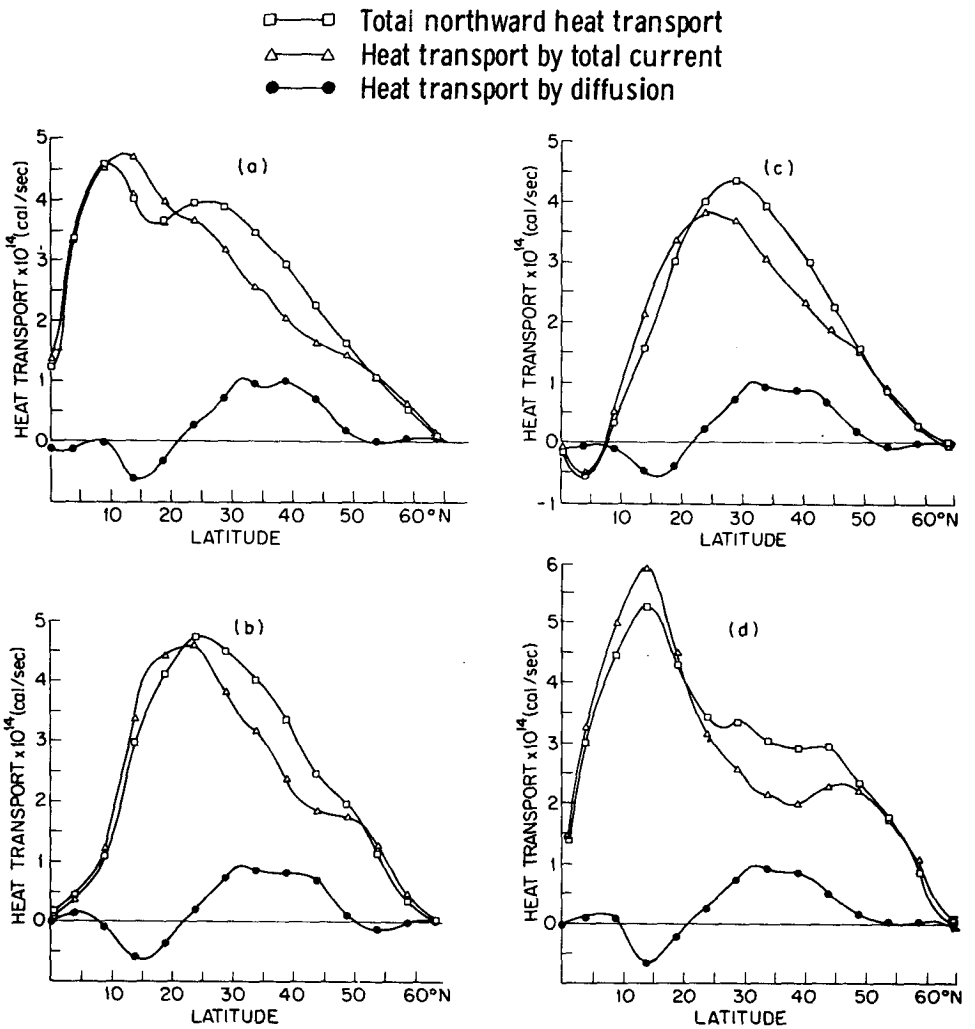

FIG. 15. The model simulated total northward transport of heat for (a) spring, (b) summer, (c) fall, (d) winter. (Note: 1 cal s^{-1} = 4.1855 W).

heat energy transported by current advection, attributed mostly to the upper layers of the ocean, is about 4.6×10^{14} cal s^{-1} (1.93×10^{15} W) near 10°N. The northern part of the North Equatorial Current flows mostly westward and the meridional transport of heat decreases poleward near 20°N. The northward flow of the North Pacific Current is strengthened in winter and more heat is transported from the subtropic region to the subarctic region. However, the east-west dimension of the North Pacific Ocean is smaller in high latitudes and so the total heat transport decreases latitudinally. As the season progresses and the whole atmospheric system shifts northward, the maximum northward transport of heat by current also shifts accordingly. The latitude of maximum advection of heat is near 25°N in fall. Notice that there is a small amount of heat transported southward from 7°N to the equatorial region. As indicated in Figs. 5c and 7c, this is the result of the weakening of the South Equatorial Current and more southern components in the Equatorial Undercurrent and in the Countercurrent.

The heat transported by diffusion is relatively small compared with the heat transported by advection in all seasons. The temperature along the equator, due to strong upwellings there, is always slightly cooler than its neighboring tropic water. A broad mass of warm water always exists in the western subtropic Pacific from 15 to 20°N. Based on the temperature distribution, the contribution from diffusion, which is always down gradient, is generally southward in low latitudes south of 20°N and northward in middle and high latitudes. Maximum northward heat transport by diffusion is around 30°N, where the maximum temperature gradient exists year round.

Most of the heat is transported in the surface layer where the current is generally the strongest and the meridional thermal gradient is the largest. The computed heat transport of the surface layer (about 20 m thick) and of the seventh layer (about 300 m thick centered at 500 m depth) are shown in Fig. 16. The negligible heat transport at the lower level confirms that most thermal energy is transported in the upper hundreds of meters in the ocean. The fact is that the heat transported by the surface layer south of 15°N is larger than the maximum of the total heat transports (Fig. 15), which means that certain subsurface layers near the equator are transporting heat in the opposite direction. It is probable that the deep equatorward transport is maintained by the barotropic advections. The largest thermal energy transport is carried out in low latitudes where, as indicated by Bryan *et al.* (1975), the thermohaline transports are in the same direction as the Ekman transports, while in the westerly zone, the thermohaline transport is against the Ekman transport. The simulated poleward heat transports are generally in good agreement with the results of Sellers (1965) and of Vonder Haar and Oort (1973), who indicate that the maximum poleward heat transport by ocean currents lies between latitudes 20° and 30°N. The simulated seasonal variation shows that the maximum heat transport in the North Pacific Ocean is between 10° and 20°N in winter and 20° and 30°N in summer.

e. Annual baroclinic long wave

The presence of the eastern boundary tends to excite baroclinic waves (Veronis and Stommel, 1956). In a recent study, White (1977) pointed out that due to an interaction of the forced annual response in the interior ocean with the eastern boundary, baroclinic long waves are generated from the east and propagate westward at phase speeds of

$$C = \frac{2g'H_0\beta}{f^2}, \tag{4.1}$$

where g' is the reduced gravity and H_0 is the mean thickness of the upper layer. Note that this baroclinic long wave is traveling at twice the speed of a nondispersive Rossby wave.

A similar baroclinic long wave is observed in the seasonal simulation. To determine the wavelength and phase speed of the annual signal, the differences between the parameter value and its longitudinal mean are plotted layer by layer at 10-day intervals for every grid latitude in the ocean model. Baroclinic long-wave phenomena show in most parameters in the tropic and subtropic areas, especially near the equator. Fig. 17 shows the consecutive time plots of the parameter u of the fourth layer (~125 m) at 11.25°N latitude at intervals of approximately 60 days. The estimated wave length of the long baroclinic wave is about 11 000 km and the phase speed is about 34 cm s^{-1}, which agrees well with the computed phase speed from (4.1) for $H_0 = 125$ m and $g' = 5.4$ cm s^{-2}. White's (1977) estimation from bathythermograph data showed that the zonal phase speed at 11°N, with an upper layer of 125 m depth, is approximately 40 cm s^{-1} and the wavelength is approximately 12 000 km. Our calculations are in quantitative agreement with White's observational results. However, there is no evidence in the simulation to indicate that phase speeds and wave lengths decrease with increasing latitudes as claimed by White (1977).

f. Energetics

As pointed out in Huang (1978), the overall sum of kinetic and potential energy in the ocean domain is conserved under the equilibrium state. We let K

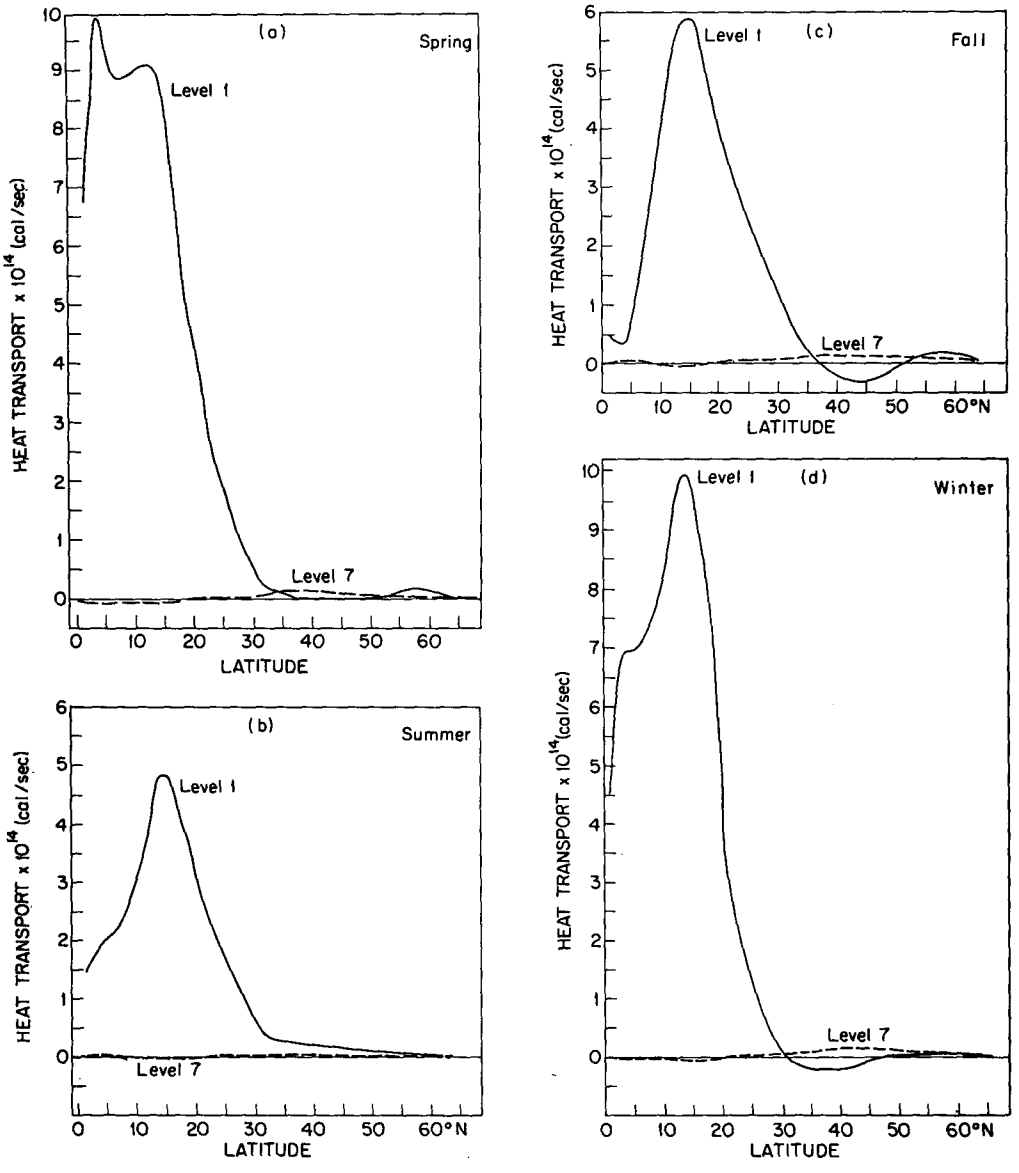

FIG. 16. The model-simulated poleward heat transport in the surface layer (20 m thick) and in the seventh layer (300 m thick centered at 500 m) for (a) spring, (b) summer, (c) fall, (d) winter. (Note: 1 cal s^{-1} = 4.1855 W).

be the total kinetic energy

$$K = \int_V \tfrac{1}{2}\rho_0 \mathbf{V}^2 dV, \tag{4.2}$$

which can be separated into two parts: one for the barotropic mode,

$$\hat{K} = \int_A \tfrac{1}{2} D \rho_0 \hat{\mathbf{V}}^2 dA \tag{4.3}$$

and one for the baroclinic mode,

$$K' = \int_V \tfrac{1}{2}\rho_0 \mathbf{V}'^2 dV, \tag{4.4}$$

where the integration subscripts V and A indicate that integrations are carried out for the whole volume and for the whole surface area, respectively, in the domain of interest. As defined in I, $\mathbf{V}$ is the horizontal velocity vector and $\hat{\mathbf{V}}$ and $\mathbf{V}'$ are the vertical mean current and the shear current, respectively. The total potential energy is computed with reference to the ocean bottom and with mean density as

$$\Phi = \int_V g(\rho_0 - \rho)(D + z) dV, \tag{4.5}$$

where z is the depth from the mean sea surface and ρ_0 the mean density.

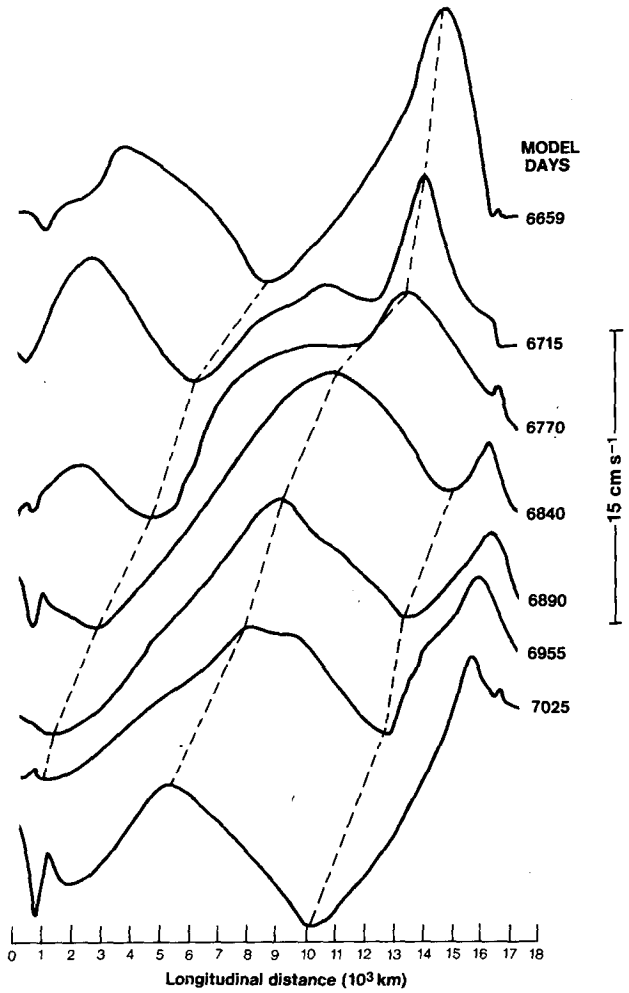

FIG. 17. Time plots of the deviations of the zonal component of velocity from its zonal mean.

Seasonal variations of the total kinetic energy, the total potential energy, the baroclinic kinetic energy and the barotropic kinetic energy are shown in Fig. 18. It is seen that the barotropic kinetic energy is about one order of magnitude smaller than the baroclinic energy, while the potential energy is about three orders of magnitudes greater than the total kinetic energy. As pointed out before, the baroclinic response is not in an equilibrium state yet and this is also shown in the Φ curve in Fig. 18. The simulated potential energy has a minimum in late winter and early spring and a maximum in late summer and early fall, lagging the seasonal heating cycle by about one month. The barotropic kinetic energy, affected mostly by the wind stress, has a maximum in winter and a minimum in late summer, lagging the wind stress cycle by about one month. The maximum kinetic energy of the baroclinic current appears in late winter and the minimum occurs in late spring. The total kinetic energy shows a maximum in winter and a minimum in early summer. Fig. 18 indicates an interesting difference between the seasonal cycle of barotropic and baroclinic kinetic energy. The barotropic kinetic energy increases during the second half of the year and decreases during the first half, while the baroclinic kinetic energy undergoes a slow buildup from late spring until the following winter, followed by a rapid decrease from winter to spring. The fact that the maximum baroclinic energy is approximately in phase with the minimum potential energy indicates that the baroclinic response in the ocean may depend more on the cooling cycle. Ocean water possesses the maximum vertically homogeneous depth in winter while the north-south horizontal density gradients are also at a maximum. Large-scale thermohaline circulations are generally in geostrophic balance. Therefore, the total baroclinic kinetic energy increases as the potential energy decreases in winter until the end of the seasonal cooling cycle. Most vertical movements cease at this time and the kinetic energy starts to decrease when the heating and stratification begin. The maximum potential energy in fall is used mostly to enhance the vertical stratification that stabilizes the ocean.

5. Summary and conclusions

Seasonal variations in the North Pacific Ocean were simulated by a baroclinic ocean model. Starting from the quasi-equilibrium state of the model after 60 years of integrations under the annual mean atmospheric forcing, integrations for the seasonal variation were carried out for another 15 years using time-dependent climatological atmospheric parameters. Although the barotropic component of oceanic current reached a seasonally quasi-equilibrium state, the baroclinic part still noticeably increased in energy after 15 years of integrations. However, the secular increase in the total baroclinic energy was less than 6% per year and the amplitude of the seasonal variation almost steady.

It is felt that the model has satisfactorily portrayed the major features and their seasonal variation in the North Pacific Ocean. The simulated seasonal fluctuation of the ocean transport function is closely related to the imposed meridional movement of the atmospheric wind forcing. In general, the simulated transport lies well within the range of observed transport. However, simulated values are closer to low estimates.

Basic features of all the major current systems in the North Pacific Ocean are reproduced in the model. The simulated surface Kuroshio is essentially steady most of the year, with a relative maximum of 64 cm s^{-1} in fall and about 60 cm s^{-1} in other seasons. Major seasonal variations appear in the upper 300 m of the ocean. The simulated

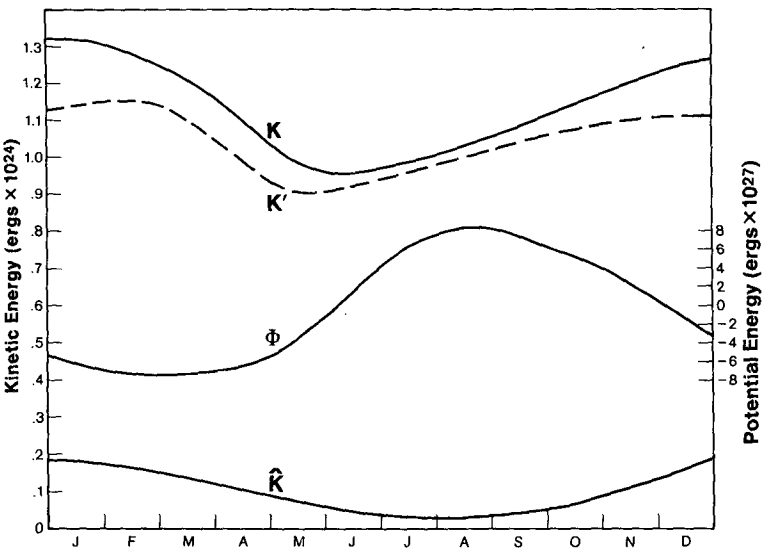

FIG. 18. Time variations of the potential energy, the total kinetic energy, the barotropic kinetic energy and the baroclinic kinetic energy. (Note: 1 erg = 2.778×10^{-14} kW·h)

Equatorial Countercurrent and Undercurrent demonstrate significant seasonal change. Both currents are strong but not as deep in fall and winter, and weak but deep in spring and summer, in agreement with the available observations. Along the North American coast, a northeastward Davison Countercurrent is also indicated during fall and winter, while the major California Current is shifted off-shore when the southerly wind appears.

The simulated surface temperature matches the observed surface temperature except in high latitudes, where it is higher than the observed temperature in winter. The discrepancy is probably attributable to the lack of long seasonal integrations to bring the model ocean to an equilibrium state so that the high latitude surface temperature in winter would be close to the deep water temperature. As the initial state of temperature in high latitudes is relatively too high, 15 years of seasonal cycles is obviously not enough to cool the temperature down to observational values. In the subsurface temperature distribution, neither the seasonal nor the main thermocline are adequately simulated.

Most of the poleward transport of heat occurs in the upper layers, especially the surface layer. The simulated seasonal variation shows that the maximum northward heat transport in the North Pacific Ocean is between 10 and 20°N in winter and between 20 and 30°N in summer.

An analysis of the basic average energetics showed that the maximum total potential energy occurs in summer and the minimum in winter, and the maximum total kinetic energy occurs in winter and the minimum in summer. The total barotropic kinetic energy variation follows the wind cycle with about a one month lag, while the total baroclinic kinetic energy variation depends mostly on the cooling cycle. The latter reaches a maximum in late winter.

The major limitations of the model, besides the lack of sufficient resolution and constant viscosities, lie in the exclusion of bottom topography and in the lack of mixed layer dynamics. The former will definitely improve the magnitude of the transport function and the latter will improve the accuracy of the prediction of the subsurface temperature structure. Another deficiency of this study is that no seasonal variation of salinity was included in the simulation because no seasonal evaporation minus precipitation data were available. Time-integrations for the seasonal simulation were not long enough to reach an equilibrium state. However, an approximate quasi-equilibrium state is achieved for most of the ocean domain and the secular change is small. It is felt that general conclusions about seasonal variations are still valid and that the present deficiencies will not adversely affect the anomaly experiments, which deal consistently with the different quantities given by the experimental results and by the corresponding seasonal state. The follow-up paper will report on the anomaly experiments in the North Pacific Ocean.

Acknowledgments. The author wishes to thank Dr. R. L. Haney for instrumental discussions and for providing the seasonal atmospheric data, Dr. W. B. White, Mr. J. F. T. Sour and L. Eber for providing oceanic observational data, Dr. C. J. Shieh for assistance and Drs. E. J. Aubert and D. B. Rao for their understanding and support.

All computations were carried out at the National Center for Atmospheric Research computing facility. The National Center for Atmospheric Research is sponsored by the National Science Foundation.

This research was supported by the Office of Naval Research for the NORPAX program through a contract with the Scripps Institution of Oceanography, University of California, and later with the University of Michigan.

REFERENCES

Allen, J., 1964: A description report on the physical and chemical properties of the northwestern Pacific Ocean during summer 1963. U. S. Naval Oceanogr. Office, Rep. No. 0-17-64.

Ballis, D., 1973: Monthly mean bathythermograph data from ocean weatherships *Papa, November, Victor*. Ref. Ser. 73-5, 73-6, 73-7, Scripps Inst. of Oceanography.

Bryan, K., 1969: A numerical method for the study of the circulation of the world ocean. *J. Comput. Phys.*, **4**, 347–376.

——, and M. D. Cox, 1968: A nonlinear model of an ocean driven by wind and differential heating: Parts I and II. *J. Atmos. Sci.*, **25**, 945–978.

——, and ——, 1972: The circulation of the world ocean: a numerical study: Part I, A homogeneous model. *J. Phys. Oceanogr.*, **2**, 319–335.

——, S. Manabe, and R. C. Paconowski, 1975: A global ocean-atmosphere climate model: Part II, The ocean circulation. *J. Phys. Oceanogr.*, **5**, 30–46.

Cox, M. D., 1970: A mathematical model of the Indian Ocean. *Deep-Sea Res.*, **17**, 47–75.

Friedrich, H. J., 1970: Preliminary results from a numerical multilayer model for the circulation in the North Atlantic. *Dtsch. Hydrog. Z.*, **23**, 145–164.

Gill, A. E., and P. P. Niiler, 1973: The theory of the seasonal variability in the ocean. *Deep-Sea Res.*, **20**, 141–177.

Gormatyuk, K. Y., and A. W. Sarkisyan, 1965: Results of four-level model calculations of North Atlantic currents. *Izv. Atmos. Oceanic Phys.*, **1**, 313–326.

Haney, R. L., 1974: A numerical study of the response of an idealized ocean to large-scale surface heat and momentum flux. *J. Phys. Oceanogr.*, **4**, 145–167.

Hata, K., 1965: Seasonal variation of the volume transport in the Oyashio area. *J. Oceanogr. Soc. Japan*, **21**, 193–201.

Holland, W. R., 1967: On the wind driven circulation in an ocean with bottom topography. *Tellus*, **19**, 582–599.

Huang, J. C. K., 1978: Numerical simulation studies for oceanic anomalies in the North Pacific basin: Part I. The ocean model and the long-term mean state. *J. Phys. Oceanogr.*, **8**, 755–778.

Jenne, R. L., H. L. Critcher, H. Van Loon, and J. J. Taljaard, 1974: Climate of the upper air: Part II, Northern Hemisphere, Vol. IV, Geostrophic winds. NCAR Rep.

Lighthill, M. J., 1969: Unsteady wind-driven ocean currents. *Quart. J. Roy. Meteor. Soc.*, **95**, 675–688.

List, R. J., 1963: *Smithsonian Meteorological Tables*. Smithsonian Institution, 527 pp.

Masuzawa, J., 1972: Water characteristics of the North Pacific central region. *Kuroshio*, H. Stommel and K. Yoshida, Eds., University of Washington Press, 517 pp (see Chap. 4).

Meyers, G., 1975: Seasonal variation in transport of the Pacific North Equatorial Current relative to the wind field. *J. Phys. Oceanogr.*, **5**, 442–449.

Miller, D. B., and R. G. Feddes, 1971: *Global Atlas of Relative Cloud Cover, 1967–1970*. NOAA, NESS, Washington, DC.

Nitani, H., 1972: Beginning of the Kuroshio. *Kuroshio*, H. Stommel and K. Yoshida, Eds., University of Washington Press, 517 pp. (see Chap. 5).

O'Brien, J. J., 1971: A two-dimensional model of the wind-driven North Pacific. *Invest. Pesquera*, **35**, 331–349.

Pedlosky, J., 1967: Fluctuating winds and the ocean circulation. *Tellus*, **19**, 250–257.

Reid, J. L., 1973: *North-West Pacific Ocean Water in Winter*. The Johns Hopkins University Press, 96 pp.

Schwartzlose, A., and J. L. Reid, 1971: Near-shore circulation in the California Current. California Cooperative Oceanic Fisheries Invest., Rep. 16, 57–65.

Sellers, W. D., 1965: *Physical Climatology*. The University of Chicago Press, 272 pp.

Sverdrup, H. U., M. W. Johnson and R. H. Fleming, 1942: *The Oceans, Their Physics, Chemistry and General Biology*. Prentice-Hall, 1087 pp.

Taft, B. A., 1972: Characteristics of the flow of the Kuroshio South of Japan. *Kuroshio*, H. Stommel and K. Yoshida, Eds., University of Washington Press, 717 pp. (see Chap. 6).

Takano, K., 1969: General circulation in the global ocean. *J. Oceanogr. Soc. Japan*, **25**, 48–50.

——, Y. Mintz and Y. J. Han, 1974: Numerical simulation of the seasonally varying baroclinic world ocean circulation. Dept. of Meteorology, University of California.

Tsuchiya, M., 1974: Variation of the surface geostrophic flow in the eastern intertropical Pacific Ocean. *Fish. Bull.*, **72**, 1075–1086.

Taljaard, J. J., H. Van Loon, H. L. Crutcher and R. L. Jenne, 1974: Climate of the upper air: Part II, Northern Hemisphere, Vol. 1, Temperature, dew points and heights at selected levels. NCAR Res. Rep.

Veronis, G., and H. Stommel, 1956: The action of variable wind stresses on a stratified ocean. *J. Mar. Res.*, **15**, 43–75.

Vonder Harr, T. H., and A. H. Oort, 1973: New estimate of annual poleward energy transport by Northern Hemisphere ocean. *J. Phys. Oceanogr.*, **2**, 169–172.

Wetherald, R. T., and S. Manabe, 1972: Response of the joint ocean-atmosphere model to the seasonal variation of the solar radiation. *Mon. Wea. Rev.*, **100**, 42–59.

White, W. B., 1977: Annual forcing of baroclinic long waves in the tropic North Pacific Ocean. *J. Phys. Oceanogr.*, **7**, 50–61.

Worthington, L. V., and H. Kawai, 1972: Comparison between deep sections across the Kuroshio and the Florida current and Gulf Stream. *Kuroshio*, H. Stommel and K. Yoshida, Eds., University of Washington Press, 517 pp. (see Chap. 10).

Wyrtki, K., 1961: Physical oceanography of the southeast Asian waters. NAGA Rep., Vol. 2. Scripps Institution of Oceanography, University of California.

——, 1965: The annual and semiannual variation of sea surface temperature in the North Pacific Ocean. *Limnol. Oceanogr.*, **10**, 307–313.

——, 1973: Seasonal variation of heat exchange and surface temperature in the North Pacific Ocean. Hawaii Institute of Geophysics Rep. HIG-66-3, 52 pp.